Synthesis of improved-quality images in the millimetre wavelength range

L.V. Volkov, A.I. Voronko, A.R. Karapetyan, S.A. Tikhomirov

Abstract. **The possibilities of quasi-optical imaging of concealed objects illuminated by millimetre wavelength range radiation are demonstrated both theoretically and experimentally. The influence of the spatial Gibbs effect and of other destructive factors on the quality of the obtained images is studied. A method is proposed for synthesising improved-quality images with enhanced information content in the millimetre wavelength range. It is shown that the theoretical and experimental results are in good agreement.**

1. Introduction

The significance of optimal active illumination of concealed objects for their quasi-optical imaging in the millimetre (MMW) and submillimetre wavelength (SMMW) regions is well known. The importance of solving this problem has increased following the development of technologies of fabricating multielement MMW sensors capable of imaging objects in the television format on the one hand [1, 2], and owing to the continuously growing significance of practical applications of the methods and systems of imaging in these wavelength regions on the other hand. Active illumination of the objects being observed solves the problem of a low contrast of passive (radiometric) images in the MMW range, which is especially important for MMW imaging indoor, and also provides the transmission of a much larger information about the concealed objects to the receiving device of the imaging system (IS) than what can be obtained by using traditional radiometric ISs.

Various approaches for obtaining active (illuminated) images of adequate visual quality and information content in various frequency ranges from microwave (37.7 GHz) to SMMW (300 GHz) frequencies have been described in papers [3–8]. The distortions of images were frequently caused by the low quality of quasi-optical elements, the

L.V. Volkov, A.I. Voronko, A.R. Karapetyan, S.A. Tikhomirov Institute of Radio Engineering and Electronics, Russian Academy of Sciences, pl. akad. Vvedenskogo 1, 141190 Fryazino, Moscow oblast, Russia;
e-mail: lvvolkov@yahoo.com

effect of speckle noise, or the secondary interference of multiply reflected radiation beams. In this work, it is shown that the quality of active MMW and SMMW images is strongly influenced by the spatial Gibbs effect. Other factors deteriorating the quality of such images are also revealed. The possibilities of high-quality imaging in a broad (MMW and SMMW) wavelength range are demonstrated both theoretically and experimentally.

2. Theoretical analysis

Our theoretical analysis of the features of imaging using partially coherent MMW and SMMW radiation will be based on the classical approach described in Ref. [9], taking into account the fact that diffraction and interference in systems intended for different applications are described quite adequately by second-order correlation functions [6, 9–11]. For an isoplanatic quasi-optical IS having a pulsed response $h(\boldsymbol{u}_i - \boldsymbol{x}_i, v)$ at a frequency v, we can write

$$G(\boldsymbol{u}_1, \boldsymbol{u}_2, v) = \int_D \int_D \mathrm{d}^2 \boldsymbol{x}_1 \mathrm{d}^2 \boldsymbol{x}_2 h^*(\boldsymbol{u}_1 - \boldsymbol{x}_1, v)$$

$$\times h(\boldsymbol{u}_2 - \boldsymbol{x}_2, v) G(\boldsymbol{x}_1, \boldsymbol{x}_2, v), \tag{1}$$

where $G(\boldsymbol{x}_1, \boldsymbol{x}_2, v)$ and $G(\boldsymbol{u}_1, \boldsymbol{u}_2, v)$ are functions of the mutual spectral density of radiation at the input and output planes of IS, respectively, $\boldsymbol{x}_i$ and $\boldsymbol{u}_i$ are radius vectors of points in these planes, and $D \times D$ is the range of definition of the function $G(\boldsymbol{x}_1, \boldsymbol{x}_2, v)$. If the separation d_1 between the lens plane and the input plane is different from the separation d_2 between the lens plane and the output plane, the radius vectors $\boldsymbol{x}_i$ and $\boldsymbol{u}_i$ in Eqn (1) should be replaced by reduced radius vectors $\boldsymbol{x}_i/d_1$ and $\boldsymbol{u}_i/d_2$, respectively.

In the following, we will assume that the radiation intensity being measured by inertial detectors at the point ξ in space is related to the mutual spectral density of radiation at this point by the expression

$$I(\xi) = \int_0^\infty \mathrm{d}v G(\xi, \xi, v). \tag{2}$$

In the general case, the mutual spectral density of radiation at the IS input should be calculated by taking into account the characteristics of radiation scattering by the object and the angular distribution of radiation for each value of frequency. It will be shown below that the features of radiation reflected from most of the objects considerably

affect the possibility of formation of high-quality spatially incoherent images.

We used test objects transmitting radiation in the MMW range to analyse separately the effect of various destructive factors on the quality of images formed in this spectral range. In this case, the intensity distribution at the IS output upon a uniform illumination of objects by quasi-monochromatic radiation with an average intensity I_0 and a central frequency v_0 (for which $\delta v \ll v_0$, where δv being the radiation linewidth) can be written in the form

$$I(\boldsymbol{u}, v_0) = I_0 \int_D \int_D \mathrm{d}^2\boldsymbol{x}_1 \mathrm{d}^2\boldsymbol{x}_2 k^*(\boldsymbol{x}_1, v_0)k(\boldsymbol{x}_2, v_0)$$

$$\times \gamma(\boldsymbol{x}_1, \boldsymbol{x}_2, v_0)h^*(\boldsymbol{u}_1 - \boldsymbol{x}_1, v_0)h(\boldsymbol{u}_2 - \boldsymbol{x}_2, v_0), \qquad (3)$$

where $k(\boldsymbol{x}_i, v_0)$ is the amplitude transmission factor of the object and $\gamma(\boldsymbol{x}_1, \boldsymbol{x}_2, v_0)$ is the degree of spatial coherence of radiation in the input plane, which is defined as

$$\gamma(\boldsymbol{x}_1, \boldsymbol{x}_2, v_0) = \frac{G(\boldsymbol{x}_1, \boldsymbol{x}_2, v_0)}{[G(\boldsymbol{x}_1, \boldsymbol{x}_1, v_0)G(\boldsymbol{x}_2, \boldsymbol{x}_2, v_0)]^{1/2}}. \qquad (4)$$

One can see from Eqn (3) that the intensity distribution at the IS output depends in the general case on the spatial coherence of the illuminating radiation.

Two limiting cases follow from Eqn (3). For illumination with complete spatial coherence $\gamma(\boldsymbol{x}_1, \boldsymbol{x}_2, v_0) = 1$, we have

$$I(\boldsymbol{u}, v_0) = I_0 \left| \int_D k(\boldsymbol{x}, v_0)h(\boldsymbol{u} - \boldsymbol{x}, v_0)\mathrm{d}\boldsymbol{x} \right|^2$$

$$= I_0 |k(\boldsymbol{x}, v_0) \otimes h(\boldsymbol{x}, v_0)|^2 = I_0 |K_{\mathrm{coh}}(\boldsymbol{u}, v_0)|^2, \qquad (5)$$

where $K_{\mathrm{coh}}(\boldsymbol{u}, v_0)$ is the normalised distribution of the complex radiation amplitude in the input plane of the IS. For spatially incoherent radiation, when $\gamma(\boldsymbol{x}_1, \boldsymbol{x}_2, v_0) = \delta(\boldsymbol{x}_1 - \boldsymbol{x}_2)$, we can write

$$I(\boldsymbol{u}, v_0) = I_0 \int_D |k(\boldsymbol{x}, v_0)|^2 |h(\boldsymbol{u} - \boldsymbol{x}, v_0)|^2 \mathrm{d}\boldsymbol{x}$$

$$= I_0 |k(\boldsymbol{x}, v_0)|^2 | \otimes h(\boldsymbol{x}, v_0)|^2. \qquad (6)$$

Expressions (5) and (6) can be used to estimate the limitations imposed on the quasi-optical imaging in the MMW and SMMW ranges. Taking into account the difference in the distances d_1 and d_2, the function $K_{\mathrm{coh}}(\boldsymbol{u}, v_0)$ can be written in the form

$$K_{\mathrm{coh}}(\boldsymbol{u}, v_0) = \alpha' F_{\boldsymbol{u}}^{-1}\left[P\left(\frac{cd_2}{v_0}\boldsymbol{\eta}\right) \exp\left[-W\left(\frac{cd_2}{v_0}\boldsymbol{\eta}\right)\right]\right.$$

$$\left. \times F_{\boldsymbol{\eta}}\left[k\left(\frac{d_1}{d_2}\boldsymbol{x}, v_0\right)\right]\right], \qquad (7)$$

where $F_{\boldsymbol{\eta}}[\ ]$ and $F_{\boldsymbol{u}}^{-1}[\ ]$ are the operators of the direct and inverse Fourier transforms in variables $\boldsymbol{\eta}$ and $\boldsymbol{u}$; $P(\xi)$ is a function describing the shape of the entrance pupil of the focusing lens (in particular, $P(\xi) = 1$ for a circular entrance

pupil for $|\xi| \leqslant L/2$ and $P(\xi) = 0$ for $|\xi| > L/2$); L is the diameter of the focusing lens; $W(\xi)$ is a function describing the radiation aberration due to imperfection of the focusing lens; and α' is a constant.

One can easily see that, if the effect of aberration function is neglected, Eqn (7) is a truncated inverse transformation, in which a part of scaled spatial spectrum of the object in the region of higher spatial frequencies is suppressed strongly by the cutoff function $P[(cd_2/v_0)\boldsymbol{\eta}]$. Taking the above-mentioned scaling into account, we can present the upper cutoff frequency for the spatial spectrum of the object image in the form

$$\Theta = \frac{Lv_0}{2cd_1}. \qquad (8)$$

Thus, a coherent IS operates as a spatial filter with a finite transmission band width ensuring a sharp cutoff of the object spectrum; consequently, its two-dimensional output signal can be described by a function with a truncated spectrum.

It is known from the theory of optical and radio-engineering systems with such pass bands that, if the input signals are described by discontinuous functions, the output signals in these systems are always distorted by unavoidable oscillations. In the general case, this effect is known as the Gibbs effect [12].

The practical application of quasi-optical systems in the MMW range is associated with the need to image mainly metal or quasi-planar plastic objects which are characterised by specular reflection of light. In this case, the distribution of the reflected radiation amplitudes will be described by the above-mentioned discontinuous functions. Let us estimate the possible consequences of the manifestation of the Gibbs effect for coherent MMW imaging systems. For this purpose, we present the transmission (reflection) coefficient of the object (quadrant) in the form

$$k(\boldsymbol{x} - \boldsymbol{x}_0) = k \prod_{i=1}^{2} Y(x_i - x_{i0}), \qquad (9)$$

where $\boldsymbol{x} = (x_1, x_2)$ is the radius vector of the points in the input plane of the IS; x_i are the Cartesian coordinates of these points; the one-dimensional function $Y(x_i)$ is the classical Heaviside step function; and k is a constant. Thus, $k(\boldsymbol{x})$ has discontinuities along the straight lines $x_1 = x_{10}$ and $x_2 = x_{20}$. For a better visualisation without any loss of generality, we assume that the entrance pupil of the lens has the shape of a square. In this case, the amplitude distribution at the output of a quasi-optical system will be described, in accordance with Eqn (7), by the truncated function:

$$K_{\mathrm{coh}}(\boldsymbol{u}) = k_0 \left(\frac{1}{2} + \frac{1}{\pi}\int_0^{(d_1/d_2)\Theta'(u_1 - x_{10}d_2/d_1)} \frac{\sin z_1}{z_1}\,\mathrm{d}z_1\right)$$

$$\times \left(\frac{1}{2} + \frac{1}{\pi}\int_0^{(d_1/d_2)\Theta'(u_2 - x_{20}d_2/d_1)} \frac{\sin z_2}{z_2}\,\mathrm{d}z_2\right), \qquad (10)$$

where k_0 is a constant, and z_i are the integration variables. The second term in each cofactor in (10) is the integral sine with the varying oscillation period depending on the upper boundary of the frequency band $\Theta = \Theta'/2\pi$ from (8) multiplied by the scaling factor realised in the IS. The

characteristic points of oscillations are optically conjugate to the points of the above-mentioned discontinuity lines. Thus, the oscillation period depends on the carrier frequency v_0 of the illuminating radiation. The general form and depth of the oscillations in the amplitude distribution (10) are preserved for any value of the carrier frequency.

For characteristic frequencies and parameters of the focusing elements in the MMW range, the spatial period of such oscillations matched to IS input taking into account the scaling factor may be as large as several centimetres, which is comparable with the size of the objects being detected with the help of such ISs. Thus, one should expect the appearance of bright spots or other false spatial structural distributions in the coherent MMW images, even for ideal (quasi-plane) objects which do not give rise to any other noise (e.g., speckle noise) distortions.

It should be noted in particular that the above-mentioned oscillations of the MMW images observed in spatially coherent radiation can also be preserved in most cases when spatially incoherent radiation is used. Herein lies one of the main differences between imaging in the optical and millimetre ranges. The matter is that the reflection of optical radiation is of diffusive type in most cases, while the MMW radiation is reflected predominantly specularly from the objects of practical interest, and the fraction of diffusely scattered radiation may be relatively small.

In this case, only a small part of the entire wide range of phase-independent partial angular components is separated from the spatially incoherent radiation [13]. This part of radiation satisfies the condition of specular reflection from the object and of the efficient capture of the reflected radiation by the entrance pupil of the IS. It is this factor that ensures a high spatial coherence of the fraction of radiation which is involved in the formation of such 'spatially incoherent' images despite the fact that the spatial coherence of the illuminating radiation in the vicinity of the object may be extremely low. Accordingly, such spatially incoherent images will be subjected to all types of distortions associated with a high spatial coherence of the imaging radiation.

This can be illustrated, in particular by the results of the experiments [5] in which a rotating mirror with a randomly scattering surface was used for spatially incoherent illumination of a metal object. However, the obtained image had a clearly manifested oscillatory structure that is not inherent in the object itself. Similar oscillatory spots were also observed in Refs [3, 4], where the departure from regularity can be explained by the combined action of the Gibbs effect and the coherent speckle noises. No spatial coherence violation was observed in Refs [3, 4]. Radiation with a high time coherence was used in all the cases considered above.

Note that such a drastic manifestation of the Gibbs effect in optics is prevented by a completely different relation between the objective pupil size and the optical radiation wavelength, which means that there is no need to consider this effect as the most significant factor responsible for distorting coherent images.

Realisation of the spatially incoherent MMW illumination taking into account the above factors is of practical importance. The appearance of the Gibbs effect is closely related to the form of the transfer function, which is described for the spatially incoherent IS by the function

$F_{\eta}[|h(x, v_0)|^2]$ in accordance with Eqn (6). This function is equivalent to autocorrelation of the above-mentioned coherent transfer function, and hence it does not have a discontinuity upon a cutoff of the spatial frequency spectrum for any form of the transfer function. This circumstance diminishes the influence of the Gibbs effect on images formed by the spatially incoherent IS.

Because coherent radiation sources tunable in a broad MMW and SMMW range are available, another efficient approach can be used for eliminating both the Gibbs effect and the effect of coherent speckle-structure noise on the image quality in active ISs. Indeed, the oscillation amplitude in Eqn (10) remains unchanged for all illumination frequencies, while the spatial period of such oscillations varies with frequency in accordance with (8). Hence, for an appropriate choice of the frequency interval, the digital or analogue storage of images corresponding to different frequencies will enhance the quality of the synthesised (resultant) image owing to a difference in their noise structures at different frequencies. Obviously, the speckle-noise structures will also be different for images obtained at different frequencies. This leads to a mutual suppression of such spatial noises upon a summation of coherent images.

The intensity distribution in such a synthesised image has the form

$$I(\boldsymbol{u}) = \sum_{i=1}^{n} \alpha(v_{0i}) I(v_{0i}) \left| F_{\boldsymbol{u}}^{-1} \left\{ P\left(\frac{cd_2}{v_{0i}} \boldsymbol{\eta} \right) \times \right. \right.$$

$$\left. \left. \times \exp\left[-W\left(\frac{cd_2}{v_{0i}} \boldsymbol{\eta} \right) \right] F_{\boldsymbol{\eta}}\left[k\left(\frac{d_1}{d_2} \boldsymbol{x}, v_{0i} \right) \right] \right\} \right|^2. \quad (11)$$

In the case of synthesis considered above, we can speak of the transformation of a certain generalised transfer function of such an IS to a smoother function, since the summation is carried out for the spectra of the same coherent image cut off by the pupil, but with a discrete increase in the effective width of the pupil function. In this case, the weight factors $\alpha(v_{0i})$ can be varied in order to compensate for the frequency dependence of the reflection coefficient or the sensitivity of the receiving array. It is also important that such a summation can be carried out only for specular images or images obtained at different frequencies for the same angles of incidence and reflection. This makes it possible to obtain high-quality images without using diffusors, by illuminating the objects directly by the transmitting antenna of the radiation source. In contrast to the spatially incoherent system, the effective time coherence of the radiation illuminating the object decreases.

Thus, any reduction in the degree of coherence leads to a decrease in the distortion of the images being formed. Obviously, the most significant improvement of the visual quality of MMW images can be attained by decreasing the spatial and time coherence simultaneously.

3. Experimental results

Fig. 1 shows the geometry of the experimental setup for multifrequency MMW imaging. A polystyrene lens with an entrance pupil diameter of 34.5 cm and a focal length of 50 cm was used as the focusing element of the quasi-optical system. A broadband multielement detector representing an array of antenna-coupled nonlinear elements designed by the authors of Refs [14–16] was used as the high-sensitive

MMW sensor of the detector [17]. The array was fabricated on a 125μm-thick microstrip of polytetrafluoroethylene. A log-periodic antenna configuration (Fig. 2) was used for each detector of the array. This ensured a broadband detection, at least in the frequency range $40-200$ GHz (the relations $R_n/r_n = \sqrt{2}$, $R_n/R_{n+1} = 0.5$, and $\alpha = 2\beta = 60°$ hold for the nth tooth of the antenna). A Schottky diode was spot-welded to each input terminal of such an antenna. In such a construction, this diode plays the role of a nonlinear transducer of currents induced on the conducting surfaces of the antenna by the incident radiation.
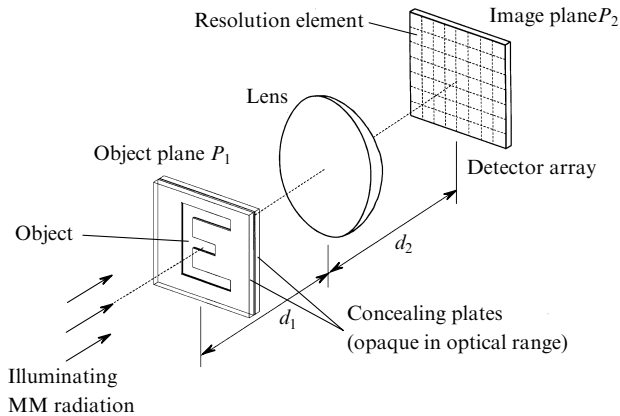
Figure 1. Schematic of the quasi-optical MMW imaging: (d_1 and d_2 are the distances from the lens to the input and output planes).
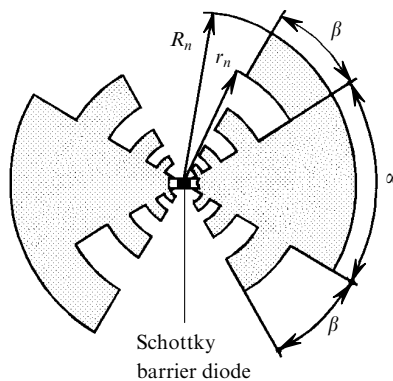
Figure 2. General view of the antenna-coupled Schottky diode as a detecting array element.

Such an array can be used for detection of radiation when an array of antenna-coupled nonlinear elements performs the amplitude detection (quadratic transformation) of the signals focused on these elements, as well as for the heterodyne detection, when the signals being received are mixed quasi-optically on a nonlinear element with a harmonic signal from an external heterodyne source employed for frequency conversion of the signals being received with a view to further amplify these signals in intermediate-frequency amplifier cascades [4, 17].

A receiver of any type (using direct detection, direct amplification and detection or superheterodyne detection) can be described by the relations presented above because the final stage of any such MMW receiver performs a nonlinear transformation of input signals followed by their

time integration through low-frequency filtration. The heterodyne transformation of a signal does not lead to any change in the structure of the temporal spectrum of the signals, but only changes their carrier frequency.

The dimensions of the arrays used were 5×5 and 8×8 elements. The array and the object were placed on additional translation stages performing computer-controlled spatial scanning of the array and the object to find the sharp image plane, to increase the information content of the images being formed, and to decrease aberrations introduced by the lens.

Amplified signals from the array elements were digitised in an analogue-to-digital converter and fed to the memory of a computer, which was used for an automatic control of the imaging system elements, image processing and visualisation.

Slit objects with different periods of the transmission function (analogue of Foucault test pattern used for testing optical and infrared systems) were used as test objects. With the help of such objects, one can easily stimulate the effect of various destructive factors on the quality of images, including a detailed elucidation of the peculiarities of the influence of the Gibbs effect on the formation of quasi-optical images in a broad MMW range.

The scheme of multifrequency imaging (Fig.1) does not contain any devices for destroying the spatial coherence of radiation, and radiation with a varying frequency illuminates the objects directly in the object plane P_1 of lens (upon normal incidence of a plane illuminating wave on the plane P_1). Backward-wave tubes OV-70, OV-71 and OV-87A, covering together the frequency range $52-178$ GHz, were used as the sources of tunable radiation. Test objects were concealed under Teflon plates of uniform thickness (2 mm) and could not be observed directly in visible light.

Fig.3 shows the one-dimensional transverse intensity distributions in the images of a four-slit periodic object with a slit width of 0.6 cm (near the diffraction limit for the lens and set of frequencies used), length 8 cm and a 6-mm gap between slits. The dashed curves show the results of numerical simulation taking into account the finite transmission band of the imaging system, having different values at different frequencies. The dotted curves show the experimental results. Fig. 3a corresponds to a frequency of 56.6 GHz, the lowest frequency in the set of discrete frequencies of the radiation illuminating the object. One can see easily that for the imaging of a four-slit object, the intensity distribution has two maxima and can be interpreted as a two-slit object. The image obtained at 79 GHz (Fig. 3b) also 'visualises' a similar 'two-slit' object with slightly displaced positions of 'false' slits. A three-slit object is observed for frequencies 92 and 104 GHz (Figs 3c and 3d), and a distribution with four maxima is observed only at frequency 135 GHz (Fig. 3e). This distribution corresponds to the real four-slit object, but the maxima in the image have different intensities for different slits. The theoretical and experimental curves are almost identical.

Thus, in the case of quasi-optical MMW imaging of periodic objects with a characteristic size of the periodic structure comparable with the diffraction limit of the focusing elements used, ghost periodic structures, whose spatial and brightness features are determined by the wavelength of illuminating radiation, may appear. It should be noted that size of details of the order of $3-10$ mm is not exotic for objects observed in the MMW imaging systems.
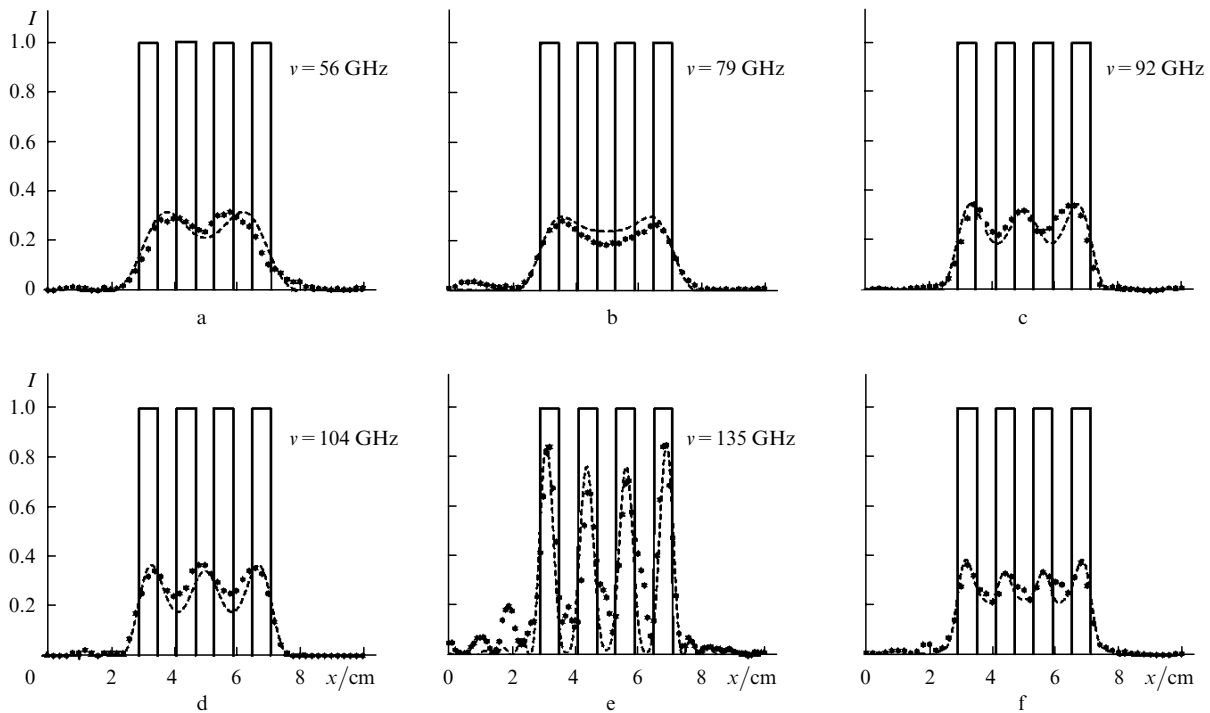
Figure 3. Experimental (points) and theoretical (dashed curve) one-dimensional intensity distributions in the images of a four-slit object (the slit width and the separation between slits is 0.6 cm, the length of the slits is 8 cm) illuminated by a completely coherent MMW radiation at various frequencies v (a–e), and the synthesised multifrequency spatially coherent image (f).

The distinguishing features of quasi-optical MMW imaging of real objects with the above-mentioned spatial dimensions are determined by the basic features of coherent imaging, which acquire a considerable practical significance in the MMW range (in contrast to the optical and even the IR range).

Fig. 3f show a synthesised image obtained by summation of signals for single-frequency images. In each pixel, the signal from the resultant synthesised image is equal to the weighted sum of signals in the corresponding pixels of the single-frequency coherent images (summation of the experimental data was carried out taking into account the difference in the sensitivities of the receiving array at different frequencies). The synthesised image obtained as a result of weighted summation of five single-frequency images provides a fairly correct image of the spatial structure as well as the brightness distribution in the object being viewed, although the contrast in this case is lower than for a single-frequency coherent imaging at a frequency of 135 GHz.

Fig. 4 shows the theoretical and experimental results of visualisation of a single-slit object whose transverse dimensional are considerably larger than the diffraction limit of the lens used. The rows in Fig. 4 correspond to single-frequency coherent images (the frequency of illuminating radiation is the same for each row, but different for different rows). One can see easily that, in this case, most images display ghost 'multislit objects', and the spatial structure of the intensity distribution in the images depends on the size of the object as well as the frequency of the illuminating radiation. Synthesised images obtained by the above technique do not suffer from these drawbacks and adequately reveal the concealed objects. A slight mismatching between the objects and their synthesised images can be attributed to

the incompleteness of the set of images with different frequencies for such a class of objects. However, the distribution of the signals resulting even from images synthesised at five frequencies provides a fairly clear idea about the transmission coefficient of objects irrespective of their transverse dimensions.

Fig. 5 shows the results of imaging of a two-slit object shaped like the latter E at various frequencies of coherent illuminating radiation. The images in the left column correspond to experimental results, while those in the right column are the results of numerical simulation. The images on the left and right sides in each row were obtained for the same frequency of illuminating radiation. As in the case of one-dimensional objects, these images display signal oscillations in both dimensions. Owing to sufficiently large transverse and longitudinal dimensions (4.7×3.5 cm) of the object, the dependence of the oscillation period on the illuminating radiation frequency is manifested clearly in accordance with formula (10). As expected, the oscillation amplitude is almost the same at different frequencies. This allows us to neutralise ghost oscillations through the summation of such images for obtaining a synthesised image of improved quality and with a richer information content.

Obviously, owing to the spatial Gibbs effect, bright spots with a clearly manifested spatial structure will emerge, as a rule, in the MMW images in a manner entirely different from that in optical systems. In this case, ghost brightness distributions will appear, which may completely distort the image even when there are no reasons for the appearance of coherent speckle noise. The effect of such distortions is enhanced in the presence of a background in the form of signals reflected from the underlying surface on which the object being observed is placed.

Fig. 6b shows a synthesised image obtained by summa-
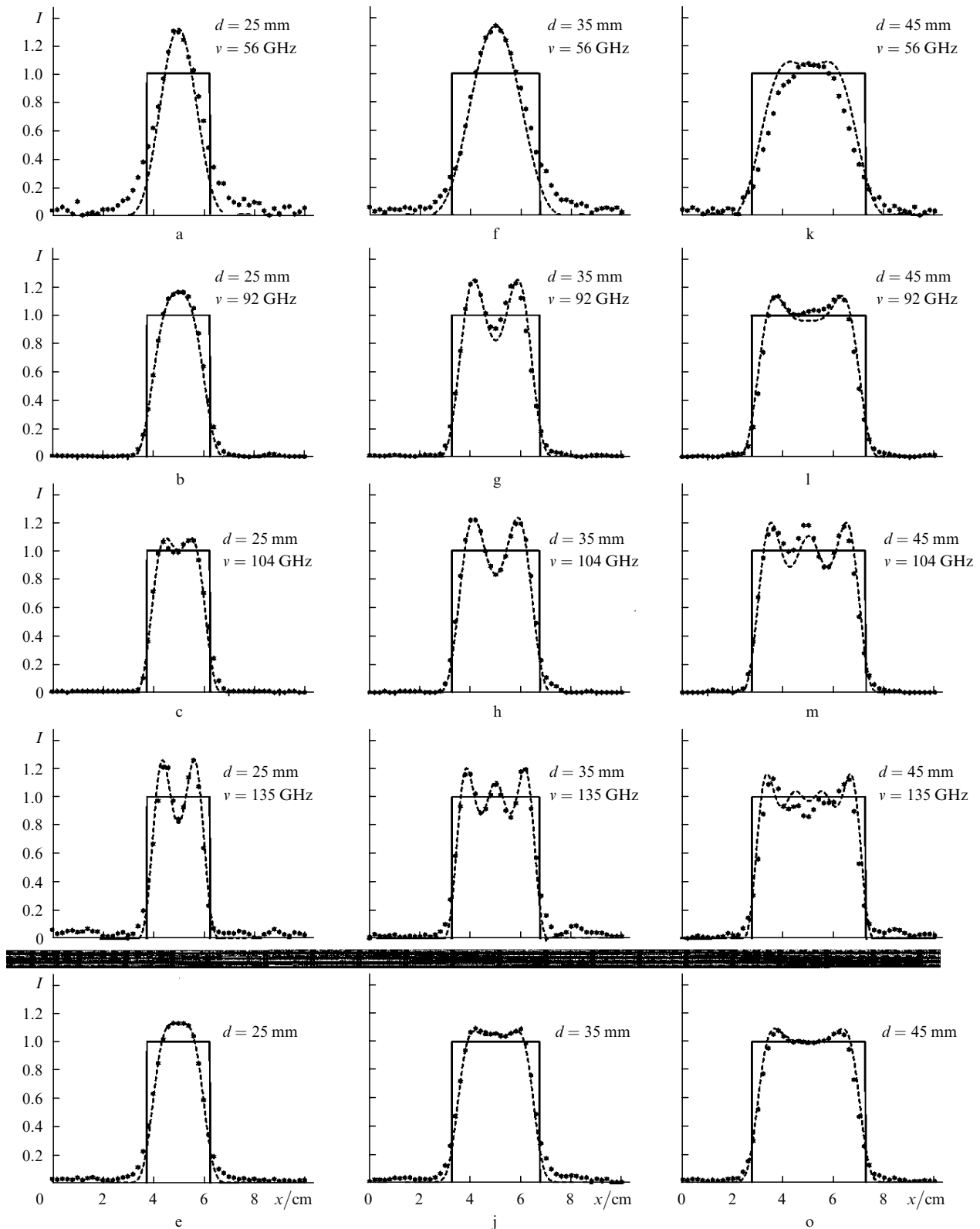
Figure 4. Experimental (points) and theoretical (dashed curve) one-dimensional intensity distributions in the images of a single-slit object having different slit widths d illuminated by a completely coherent radiation at various frequencies v (a–d, f–i, k–n) , and the synthesised multifrequency spatially coherent image (e, j, o).

tion of experimental images formed at frequencies 56–135 GHz. The same image obtained as a result of synthesis of theoretical images formed at the same frequencies is
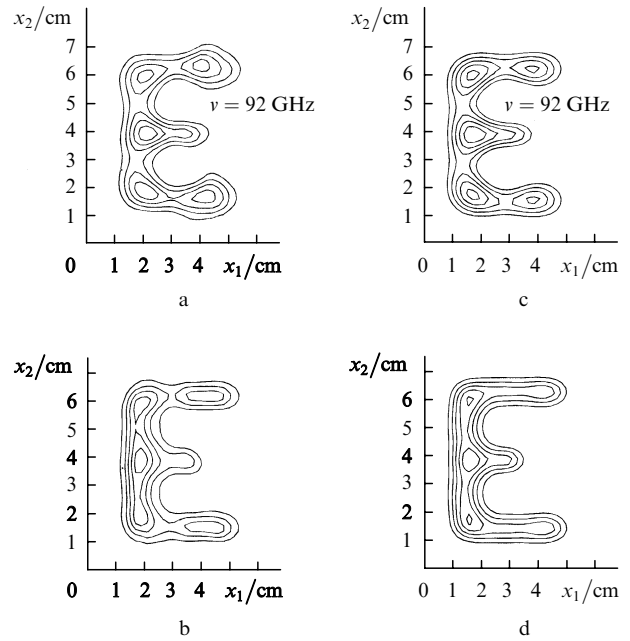
shown in Fig. 6d (the images formed at a frequency 92 GHz are not shown in Fig. 5). For comparison, the single-frequency images obtained at a frequency 92 GHz are
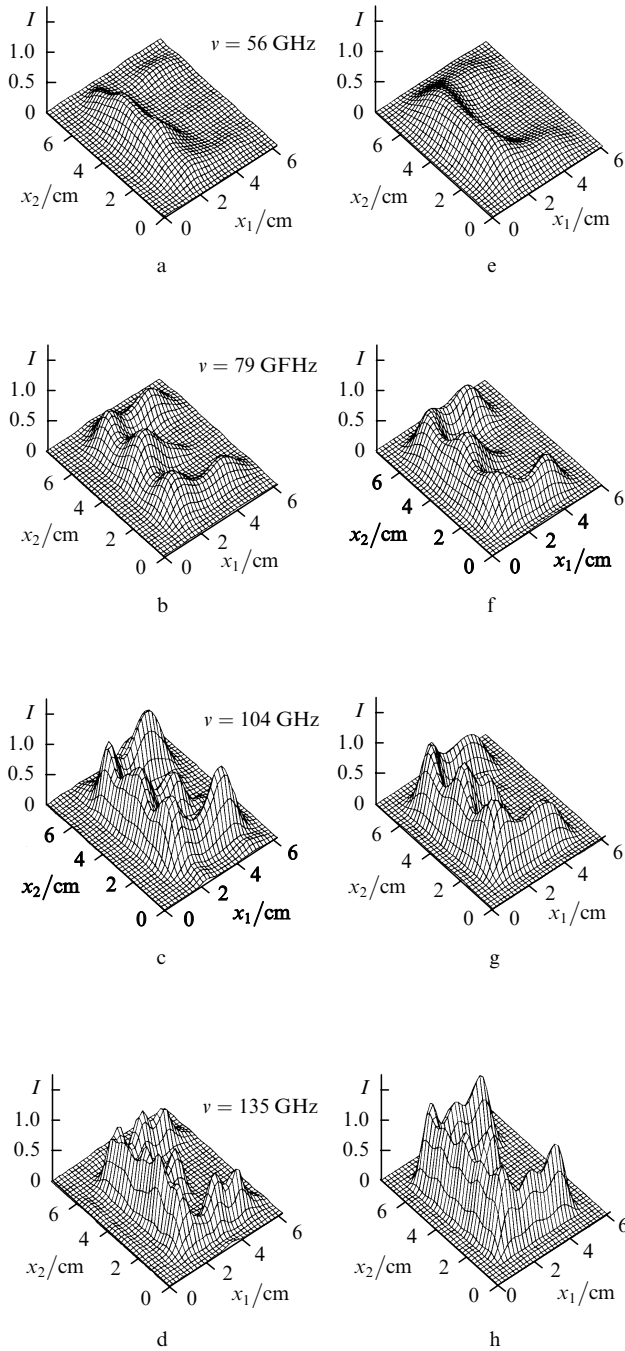
Figure 5. Two-dimensional intensity distribution in images of the letter E, obtained by using completely coherent radiation intensity at various frequencies v (a–d), and the results of numerical simulation (e–h).


Figure 6. Experimental (a, b) and theoretical (c, d) contour intensity distributions in images of the letter E for single-frequency spatially coherent images at frequency 92 GHz (a, c), and the synthesised five-frequency spatially coherent images (b, d).
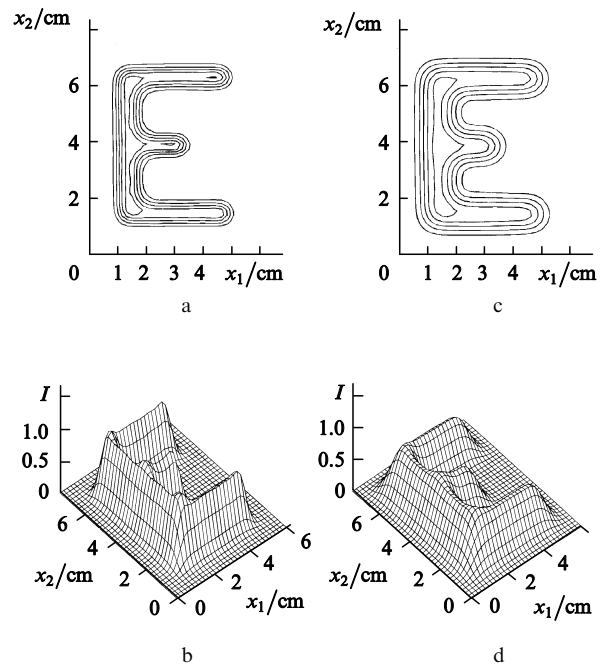
Figure 7. Results of numerical simulation for two types of images of the letter E: synthesised multifrequency spatially coherent images (a, b) and spatially incoherent monochromatic image (c, d).

presented in Figs 6a and c. One can clearly see that the quality of synthesised images is considerably enhanced since the oscillatory vibrations of brightness signals are considerably suppressed in them and the bright spots characteristic of single-frequency images are absent altogether.

An increase in the frequency bandwidth will naturally improve the quality of synthesised multifrequency images, which may become higher than that of spatially incoherent single-frequency images. For example, Fig. 7 shows the results of numerical simulation of a synthesised multifrequency image obtained in the frequency range 70–200 GHz

by storing single-frequency coherent images with a frequency step of 5 GHz. Figs 7c and d show the results of numerical simulation of an image obtained in spatially incoherent radiation at frequency 92 GHz [in accordance with formula (6)]. One can easily see that the distribution of spatial brightness is almost the same for both images, but the size of the typical features for the synthesised image has
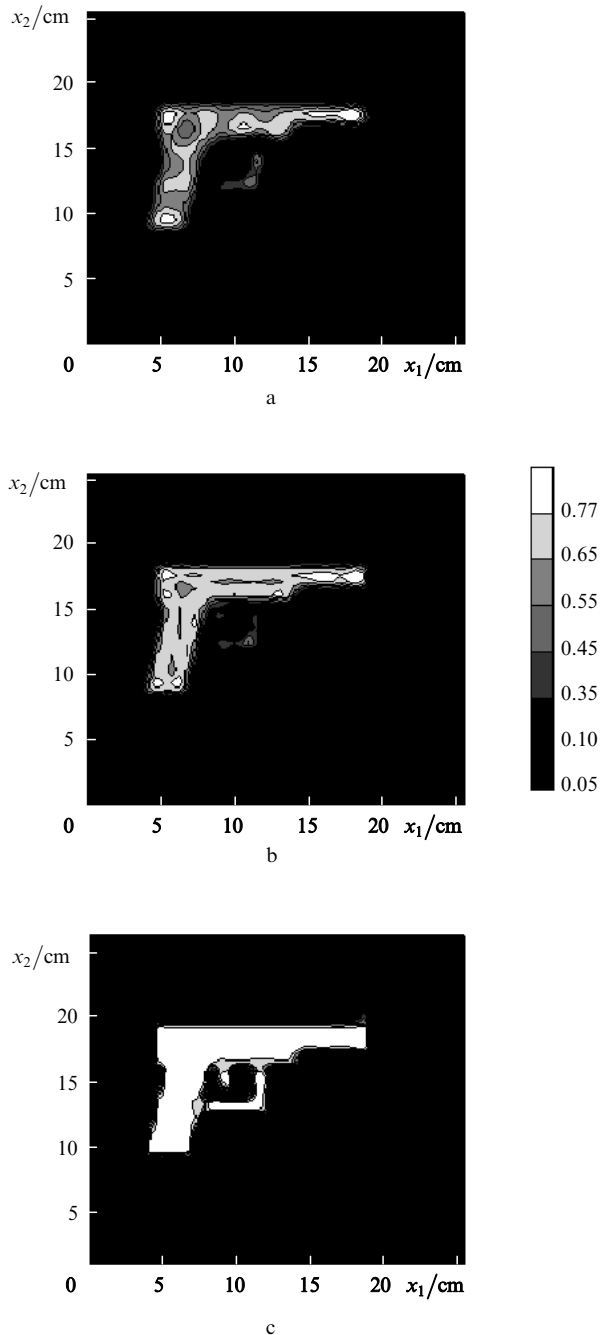
Figure 8. Numerical simulation of images of a model object: single-frequency coherent images at frequency 70 GHz (a), synthesised five-frequency image for a set of frequencies 68, 76, 84, 92, and 100 GHz (b), and synthesised multifrequency image in the frequency range 68 – 268 GHz with a frequency step of 10 GHz (c).

a closer correspondence to the object size (in other words, the sharpness of the synthesised image is higher).

Thus, the principle of multifrequency image storage for synthesising images with an improved visual quality has been confirmed theoretically and experimentally for all the objects considered here. The experimental and theoretical results were found to be in good agreement within the errors of measurement.

To illustrate the practical significance of the above effects for identifying objects, Fig. 8 shows the results of numerical simulation of an object whose shape and characteristic dimensions of details are similar to those of typical objects for which the MMW imaging system is developed.

The distribution of brightness spots in Fig. 8a corresponds to the structure of spots in the images of real pistols obtained experimentally in Refs [3, 4]. It should be emphasised that the calculations did not take into account any factors that could cause speckle distortions of images, although the structure of the intensity distribution presented in Fig. 8a resembles a speckle image. A correct understanding of the factors responsible for distortion of images of real objects makes it possible to work out appropriate methods for their elimination. The multifrequency MMW imaging may serve as one of such methods. The quality of the synthesised image in Fig. 8b, which is formed as a result of summation of only five single-frequency images, is already considerably improved. Fig. 8c provides an adequate image of the object, as was observed for the objects considered earlier (both in experiments and in numerical simulation).

Obviously, the multifrequency synthesis will also reduce efficiently the level of speckle noise in coherent images of objects with a rough or nonuniform surface. This is due to the fact that the structure of speckles (aventurine spots) in single-frequency images obtained at considerably different frequencies will have statistically different spatial distributions, which will provide a mutual suppression of such spots in the resulting synthesised image for an appropriate choice of the frequency band and frequencies of the radiation illuminating the object.

References

1. Yujiri P.L., Fornaca S., et al. *Proc. SPIE Int. Soc. Opt. Eng.*, **3378**, 14 (1998).
2. Kuroda R.T., Dow G.S., et al. *Proc. SPIE Int. Soc. Opt. Eng.*, **3378**, 57 (1998).
3. Lluukanen At., Viitanen V.-P. *Proc. SPIE Int. Soc. Opt. Eng.*, **3378**, 36 (1998).
4. Goldsmith P.F., Hsieh C.T., Huguenin G.R., et al. *IEEE Transaction on Microwave Theory and Techniques*, **41**, 1664 (1993).
5. Zverev V.A., Stepanov N.S. (Eds) *Eksperimental'naya radiooptika* (Experimental Radiooptics) (Moscow: Nauka, 1979).
6. Volkov L.V., Tikhomirov S.A. *Radiotekh. Elektron.* (3), 513 (1994).
7. Volkov L.V., Voronko A.I., Tikhomirov S.A. *Proc. SPIE Int. Soc. Opt. Eng.*, **2558**, 421 (1995).
8. Volkov L.V., Lyubchenko V.E., Tikhomirov S.A. *Proc. of the Intern. Conf. on Computional Electromagnitic and its Applications (ICCEA'94)* (Beijing, Chine, 1994) pp 548-551.
9. Perina J. *Coherence of Light* (London: Butterworths, 1972; Moscow: Mir, 1974).
10. Volkov L.V., Larkin A.I. *Kvantovaya Elektron.*, **21**, 375 (1994) [*Quantum Electron.*, **24**, 350 (1994)].
11. Larkin A.I., Volkov L.V. *Proc. III Intern. Conf. of the International Society on Optics Within Life Sciences* (Tokyo, Japan, 1994).
12. Goodman J. *Introduction to Fourier Optics* (New York, 1968; Moscow: Mir, 1970).
13. Friberg A., Wolf E. *Opt. Acta*, **30**, 1417 (1983).
14. Volkov L.V., Lyubchenko V.E., Tikhomirov S.A. *Proc. III Europ. Gallium Arsenide Applications Symposium (GAAS'94)* (Torino, Italy, 1994) pp 97 – 100.

15. Volkov L.V., Lyubchenko V.E., Tikhomirov S.A. *III Intern. Conf. on Millimeter Wave and Far-infrared Science and Technology (ICMWFST'94)* (Guangzhou, China, 1994) pp 355 – 358.
16. Volkov L.V., Lyubchenko V.E., Tikhomirov S.A. *Radiotekh. Elektron.*, **40**, 322 (1995).
17. Rebeiz G.M. *Proc. IEEE*, **80**, 1748 (1992).